FRONTIERS OF PHYSICS

RESEARCH ARTICLE
Volume 21 / Issue 6 / 064202 / 2026

Tunable C_2 selectivity in CO electroreduction via charge-asymmetric dual-metal catalysts on ferroelectric In_2Se_3

Dongqiu Zhao[1], Xiao Tang[2], Yixin Zhang[1], Shuli Liu[1], Di Yuan[1], Chen Long[1], Lin Ju[1,†], Liangzhi Kou[3,‡]

1 School of Physics and Electric Engineering, Anyang Normal University, Anyang 455000, China
2 College of Science, Nanjing Forestry University, Nanjing 210037, China
3 School of Mechanical, Medical and Process Engineering, Queensland University of Technology, Brisbane QLD 4001, Australia
Corresponding authors. E-mail: †julin@aynu.edu.cn, ‡liangzhi.kou@qut.edu.au
Received October 12, 2025; accepted November 10, 2025

© Higher Education Press 2026

ABSTRACT

The development of efficient catalysts for the electrocatalytic CO reduction reaction toward high-value C_2 products is critical for addressing pressing energy and environmental challenges. Dual-metal catalysts have emerged as promising candidates due to their potential to facilitate C–C coupling, a key step in C_2 product formation. However, their activity and selectivity are highly dependent on the charge states of the active sites. Modulating asymmetric charge distribution between metal centers offers a viable strategy to enhance C–C coupling efficiency and product selectivity. In this study, we employ density functional theory to investigate heteronuclear dual-atom catalysts (DACs) anchored on ferroelectric In_2Se_3 and impact of polarization on charge states of metal sites. We find that Pd–Nb and Rh–Nb DACs form spatially separated charge centers with opposite signs, which significantly reduce the energy barrier for C–C coupling compared to homonuclear Nb–Nb DACs, enabling thermodynamically favorable C–C bond formation. The Coulomb interaction between oppositely charged centers is identified as a key descriptor governing C–C coupling efficiency. Furthermore, ferroelectric polarization switching of In_2Se_3 offers dynamic modulation of reaction pathways and product selectivity. Pd–Nb@In_2Se_3 under downward polarization (P↓) favors ethane formation with a limiting potential of –1.06 eV, whereas upward polarization (P↑) shifts the reaction toward an alternative C–C coupling pathway with a higher overpotential (–1.47 eV). Similarly, Rh–Nb@In_2Se_3 selectively produces ethanol under P↓, but methane under P↑. Importantly, both Pd–Nb and Rh–Nb DACs exhibit stronger CO adsorption than H adsorption, favoring CORR over the competing hydrogen evolution reaction. These findings underscore the potential of ferroelectric DACs as tunable and selective catalysts for CORR, offering a compelling strategy for the rational design of next-generation electrocatalysts for decarbonization.

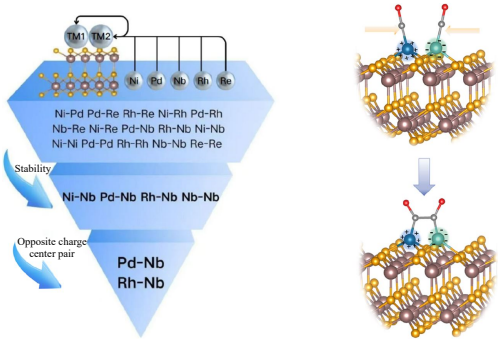

Keywords electrocatalysis, CO reduction reaction, dual-atom catalysts, polarization switch, C_2 product

*Special Topic: Electrocatalysis in Energy Conversion and Storage (Eds.: Jie Li, Haiqing Zhou, Ming Zhang & Min Liu).

Higher Education Press

https://doi.org/10.15302/frontphys.2026.064202

1 Introduction

In recent years, renewable energy driven chemical processes, such as CO_2 reduction reaction [1, 2], nitrogen reduction reaction [3], overall water-splitting reaction [4, 5], hydrogen evolution reaction [6, 7], and oxygen evolution reactions [8] are now viewed as environmentally friendly and sustainable pathways for producing valuable chemical products. The viability of the electrocatalytic synthesis hinges largely on the performance of the electrocatalysts involved. Hence, the development of high-performance and economically viable electrocatalysts is crucial for enabling their widespread practical implementation [9]. Single-atom catalysts (SACs) exhibit significant advantages in the field of electrocatalytic CO_x reduction due to their unique metal-ligand atomic electronic structure [10, 11]. However, the spatial isolation properties between SAC active sites result in a product selectivity that is usually limited to the C_1 product, such as CO [12, 13] and CH_4 [14]. The C_2 products, including C_2H_4 [15], C_2H_5OH [16, 17], and C_2H_6 [18], are characterized by their higher energy density and industrial application value. However, the synthesis of C_2 products involves complex processes with multi-electron transfer and C–C coupling, and its reaction energy barrier is significantly higher than that of the C_1 product generation pathway [19]. In recent years, it has been shown that the issue can be effectively solved by introducing synergistic catalytic sites through the construction of dual-atom catalysts (DACs) [20–23]. Unlike SACs where isolated sites typically limit products to C1 species, the paired active sites in DACs can accommodate more complex reaction pathways, providing the spatial flexibility and multi-site synergy crucial for C–C coupling. This unique advantage is evidenced by recent experimental advances. For instance, dual-copper-site catalysts have been shown to promote ethylene formation with a Faradaic efficiency of 52% during CO_2 electroreduction [24], while asymmetric In–Cu and Ni–Co dual-atom pairs have achieved high selectivity (up to 92%) for C_2 products in photocatalytic CO_2 reduction [25, 26]. Since synergistic effect of metal atoms with different valence states can promote C–C coupling [27–29], it is believed that dimers composed of different metal atoms in bimetallic DACs can provide functional active sites for C_2 production. By selecting different metals, the net charge difference between metal atoms in the dimer can be regulated to facilitate C–C coupling and potentially enhance selectivity toward C_2 products. Currently, the dominant bimetallic DACs are two-dimensional nitrogen-doped carbon materials such as Fe–Co bisites [30], Ni–Fe bisites [31], and Co–Pt bisites [32]. Their catalytic performances are highly dependent on the microstructure and coordination of the DACs, and can be improved by external fields or doping, which is however a high energy costing and challenging process. Recent theoretical and experimental works have demonstrated that, the adjustable polarization direction in ferroelectric materials is an alternative and visible strategy to modulate the catalytic activity of their surfaces and the final reaction products [4, 33–35]. Different from single atom anchored ferroelectric substrate, in DACs the polarization is expected to not only modulate the charge transfer from substrate to the metal, but also regulate the asymmetric charge distributions among two metal sites to facilitate C–C coupling and tune C_2 product selectivity.

In this study, we anchor dual transition metal atoms on the surface of ferroelectric α-In_2Se_3 monolayer to form ferroelectric DAC. The theoretical calculations demonstrate that the positive and negative charge center pair (PNCCP) is formed between the two transition metal (TM) atoms, which can effectively lower the energy barrier of C–C coupling for C_2 productions. Besides, the switched polarization can not only tune the reaction barrier and path of CO reduction reaction (CORR), but also lead to different final products due to the modulated charge states among the metal sites. These findings unveil the potential of ferroelectric DACs as tunable and selective catalysts for CORR, offering a feasible strategy for rational electrocatalysts design to produce high-value fuels.

2 Methods

The density functional theory (DFT) calculations are performed with the Vienna ab initio simulation package (VASP) code [36, 37]. The spin-polarized generalized gradient approximation (GGA) in the form of Perdew–Burke–Ernzerhof (PBE) treats the exchange–correlation interactions, while the frozen-core projector augmented wave (PAW) approximation describes the interaction between the ion and electron [38–40]. The van der Waals (vdW) interactions are described with the DFT-D3 method in Grimme's scheme [41]. Two TM atoms are distributed on two adjacent hexagonal centers of 4 × 4 In_2Se_3 supercells, which act as catalytic active sites. The dipole correction is taken into account for all the asymmetric structures [42]. The 2D Brillouin sampling is presented with a 1 × 1 × 1 gamma-centered Monkhorst-pack k-mesh. To ensure that the periodic images in the non-periodic direction do not interact with each other, a vacuum region of more than 20 Å is reserved. The cutoff energy for plane-wave basis sets is 500 eV. The convergence thresholds for force and total energy are 10^{-2} eV/Å and 10^{-5} eV, respectively. The site-specific charge differences are obtained using Bader analysis. Besides, when calculating the Gibbs free energy of CORR, we consider the solvent effect by using the implicit water solvent model implemented in VASPsol [34, 43], with a relative dielectric constant of 80 to represent the aqueous environment. More details of the simulations on Gibbs free energy can be found in the Supporting Information. In particular,

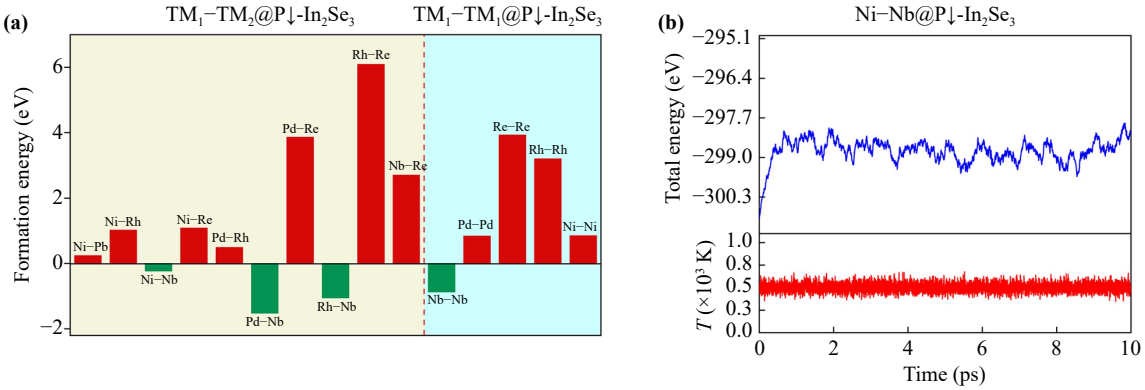

Fig. 1 **(a)** The formation energies of ten TM_1–TM_2@P↓-In_2Se_3 and five TM_1–TM_1@P↓-In_2Se_3 models (TM_1, TM_2 = Ni, Pd, Rh, Nb, and Re). **(b)** AIMD simulations of the Ni–Nb@P↓-In_2Se_3 configuration at 500 K, showing the fluctuations of the total energy (upper) and temperature (lower) over a time step of 1 fs and a duration of 10 ps.

for all calculations in this work, the thermodynamic state of the product H_2O is defined as the liquid phase at 298.15 K.

3 Results and discussion

3.1 Configurations of ferroelectric DACs

The van der Waals layered α-In_2Se_3, a two-dimensional room-temperature ferroelectric semiconductor, is selected as the substrate. This material exhibits robust structural stability under ambient conditions and has been successfully synthesized experimentally [44]. Notably, its switchable spontaneous polarization with reversible behavior at 300 K has been unequivocally validated through piezoresponse force microscopy [44]. As shown in Fig. S1, the polarization orientation, locked by the inherent asymmetry in the quintuple-layer stacking configuration, can be inverted via displacement of the central selenium atoms within the lattice [35, 45]. The heteronuclear and homonuclear ferroelectric DACs (TM_1–TM_2@In_2Se_3 and TM_1–TM_1@In_2Se_3) are constructed with the ferroelectric In_2Se_3 substrate anchored with TM atoms. According to our previous work [35], only five types of single TM atom anchored In_2Se_3 monolayer (TM@In_2Se_3, TM = Ni, Pd, Rh, Nb, and Re) are stable [35]. Therefore, in this work we select these five TM atoms to construct ten heteronuclear TM_1–TM_2@In_2Se_3 and five homonuclear TM_1–TM_1@In_2Se_3 models. Under the configuration of downward polarization (P↓), we investigate the stability of these ferroelectric DACs initially based on the formation energy (E_{for}), which is obtained with Eq. (ES1) in the Supporting Information. Based on the definition, the configurations with a negative formation energy are synthesizable. Therefore, three TM_1–TM_2@P↓-In_2Se_3 hetero-configurations (Ni–Nb, Pd–Nb, and Rh–Nb) and Nb–Nb@P↓-In_2Se_3 homo-configuration are preliminarily screened out as candidate catalysts [Fig. 1(a)]. As listed in Table S1 for the P↑ situation, although the TM_1–TM_2@P↑-In_2Se_3 hetero-configurations (Ni–Nb, Pd–Nb, Rh–Nb) and the Nb–Nb@P↑-In_2Se_3 homo-configuration exhibit positive formation energies, their desorption energies are very high (>10 eV). Consequently, once synthesized in the P↓ state, polarization reversal cannot dislodge the single TM atoms from the In_2Se_3 surface in these heteronuclear and homonuclear ferroelectric DACs. To further demonstrate the structural stability of these candidates, we employ molecular dynamics simulation (AIMD) calculations on Ni–Nb@P↓-In_2Se_3 model, which has the highest formation energy among these four ferroelectric DACs in the P↓ state. AIMD simulations are conducted at temperature of 500 K, with a time step of 1 fs, and a total time length of 10 ps. During the AIMD simulations, the geometrical structure remains intact, indicating that Ni–Nb@P↓-In_2Se_3 has good thermal stability [see Figs. 1(b) and S2]. Overall, both the formation energy and molecular dynamics simulations promise the structural stability of these four ferroelectric DAC configurations. Regarding experimental realization, the synthesized DACs (e.g., Pd–Nb@In_2Se_3 and Rh–Nb@In_2Se_3) could potentially be achieved via advanced techniques such as atomic layer deposition [46, 47] or wet chemical synthesis [48], which have proven effective in creating tailored dual-metal sites on various substrates.

3.2 Positive and negative charge center pair in the ferroelectric DACs

Previous reports have indicated that the occurrence of C–C coupling reactions can be effectively promoted if the bimetallic sites in DAC can form PNCCP on the substrate. Therefore, we next screen the samples that can form the PNCCP, from the three TM_1–TM_2@In_2Se_3 configurations (Ni–Nb, Pd–Nb, and Rh–Nb). As listed in Table S2, in the Pd–Nb@In_2Se_3 and Rh–Nb@In_2Se_3

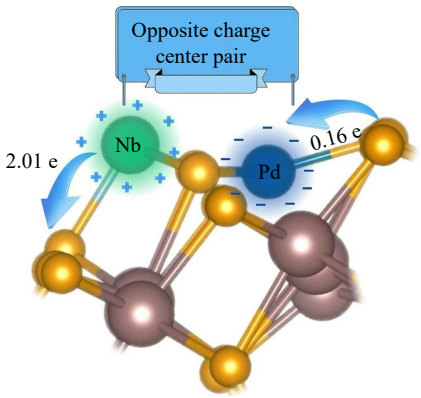

Fig. 2 The PNCCP formed through electron transfer between the TM single atoms and substrate in Pd–Nb@P↓-In_2Se_3 system.

configurations, the adsorbed TM_1 and TM_2 single atoms gain and lose electrons respectively, to form PNCCP. Taking Pd–Nb@P↓-In_2Se_3 as an example, the adsorbed Nb single atom donates 2.01 electrons to the substrate, forming a positive charge center, while the Pd single atom accepts 0.16 electrons from the substrate, forming a negative charge center (as shown in Fig. 2). Consequently, the Nb–Pd dual-atom pair constitutes an opposite charge center pair. Similarly, in Pd–Nb@P↑-In_2Se_3, the adsorbed Nb atom donates 1.87 electrons to form a positive charge center, whereas the Pd atom accepts 0.15 electrons to form a negative charge center. Therefore, while polarization reversal modulates the intensity of the opposite charge center pair via reversal of the internal electric field, it does not alter the charge sign of the pair. This is clearly demonstrated in the Rh–Nb system, where the electron gain at the Rh site decreases from 0.24 in the P↓ state to 0.11 in the P↑ state, while the electron donation from its Nb partner changes from –1.96 to –2.07. Subsequently, we employ the Pd–Nb@In_2Se_3 and Rh–Nb@In_2Se_3 systems to investigate whether PNCCP could effectively promote C–C coupling, along with examining the effect of polarization switching on their CORR catalytic performances.

3.3 Tunable CORR catalytic performance by polarization switching

The switchable polarization within ferroelectric materials significantly affects the electronic structure of the catalyst by modulating the *d*-band center position [35]. When the ferroelectric substrate undergoes a polarization flip (see Fig. S3), its surface stoichiometry ratio and the electronic environment of the adsorption site are reconfigured, resulting in the significantly changed adsorption energy of CO molecules (ΔG_{*CO}) and energy barrier of the C–C coupling. Therefore, it is expected that the reaction barriers, reaction paths, and even the intermediate and final products of CO reduction could be controlled by ferroelectric switching. As illustrated in Fig. S4, we systematically explore the lowest-energy pathways for CORR across Pd–Nb and Rh–Nb DACs under different polarization states. Table 1 summarizes the effect of polarization switching on CORR in terms of C–C coupling type, potential-determined hydrogenation steps, limiting potential and final products.

The electrochemical CORR over the Pd–Nb@P↓-In_2Se_3 catalyst follows the reaction pathway illustrated in Fig. 3(a). The process begins with the adsorption of CO molecules onto the Pd site of catalyst surface (denoted as CO*), where the Pd–Nb bimetallic sites play a critical role in stabilizing the adsorbed species. Subsequently another CO adsorption at the Nb site (CO*+CO → CO*CO*) is facilitated by synergistic electronic interactions between Pd and Nb, but the two C atoms from the two adsorbed CO molecules are not bonded. First hydrogenation of the CO group is preferred at the Pd site to form a CO*CHO* intermediate (CO*CO* + H^+ + e^- → CO*CHO*). It is interesting to notice that the hydrogenation at Pd site will enable C–C coupling reaction (CO*CHO* → COCHO*), which is thermodynamically favorable (exothermic). After that, the second hydrogenation of the intermediate species COCHO* leads to the formation of glyoxal (CHOCHO*) (COCHO* + H^+ + e^- → CHOCHO*). Then one carbonyl group (C=O) in CHOCHO* undergoes selective hydrogenation. A hydrogen atom binds to the oxygen atom, forming a hydroxyl group (–OH), which generates the intermediate of CHOHCHO* (CHOCHO* + H^+ + e^- → CHOHCHO*). Subsequently, the remaining carbonyl group is fully hydrogenated, leading to the formation of the diol intermediate CHOHCHOH* (CHOHCHO* + H^+ + e^- → CHOHCHOH*), and $CHOHCH_2OH$* ($CHOHCHOH$* + H^+ + e^- → $CHOHCH_2OH$* + H_2O). This $CHOHCH_2OH$* intermediate then progresses through further deoxygenation and

Table 1 The C–C coupling type, potential determining step (PDS), limiting potential (U_l vs. RHE), and final product of CORR with Pd–Nb@In_2Se_3 and Rh–Nb@In_2Se_3 catalysts under different polarization states.

Catalyst	C–C coupling	PDS	U_l	Product
Pd–Nb@P↓-In_2Se_3	CO*CHO*→COCHO*	CH_2CH_2*→CH_2CH_3*	–1.06	C_2H_6
Pd–Nb@P↑-In_2Se_3	CO*CO*→COCO*	CH_2CHOH*→CH_2CH_2OH*	–1.47	C_2H_6
Rh–Nb@P↓-In_2Se_3	CO*CHO*→COCHO*	CH_2CHO*→CH_2CHOH*	–0.98	CH_3CH_2OH
Rh–Nb@P↑-In_2Se_3	–	CHO*→HCOH*	–0.35	CH_4

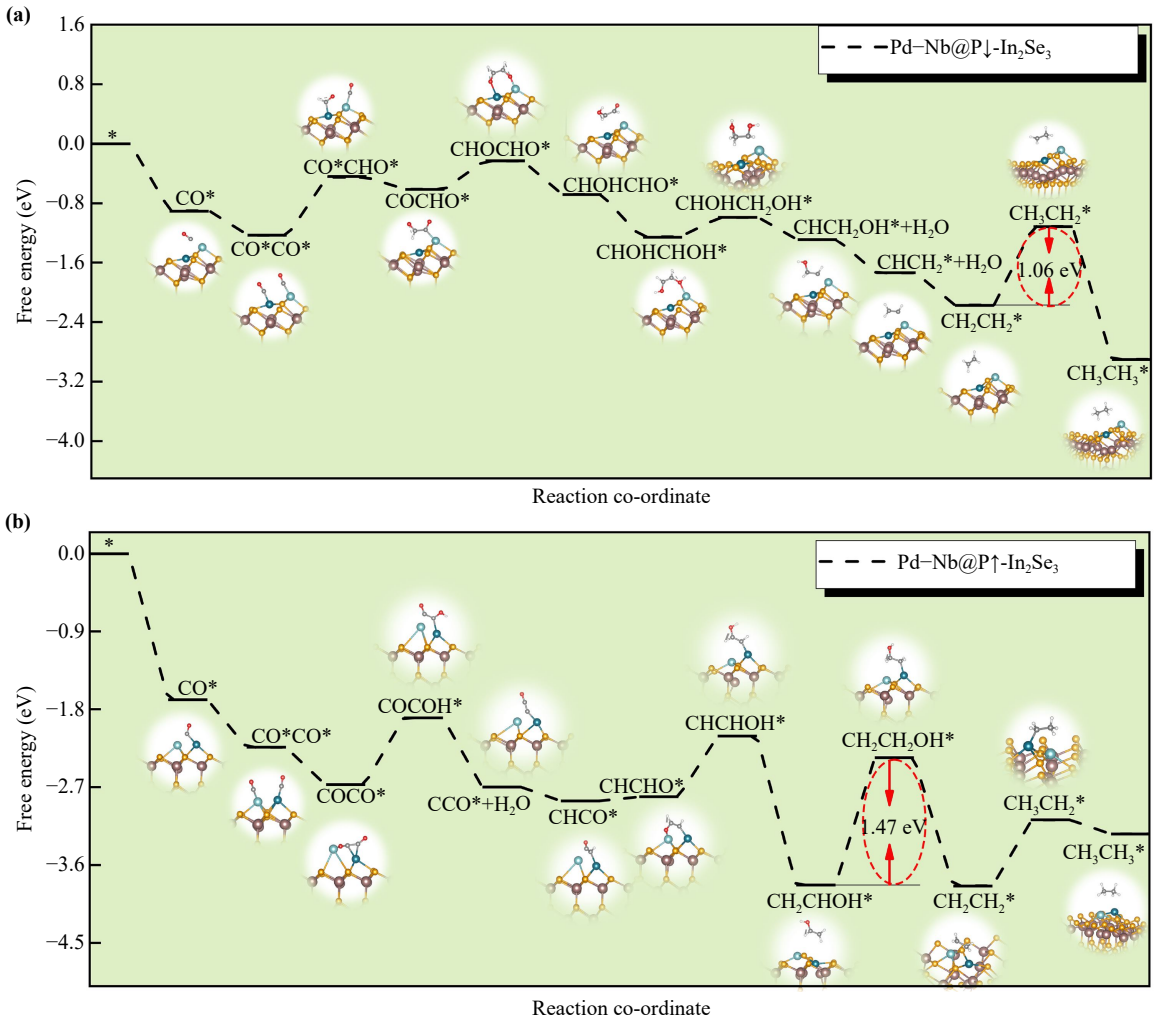

Fig. 3 Free energy distribution of the CORR on **(a)** Pd–Nb@P↓-In_2Se_3 and **(b)** Pd–Nb@P↑-In_2Se_3 along the minimum energy path at 0 V (vs. RHE). The inset shows the optimized configurations of the intermediates.

condensation steps: $CHOHCH_2OH^*$ loses an oxygen atom to form $CHCH_2OH^*$ ($CHOHCH_2OH^* + H^+ + e^- \rightarrow CHCH_2OH^* + H_2O$). H_2O will be produced and released after hydroxyl group combining with H^+. $CHOHCH_2OH^*$ generate $CHCH_2OH^*$($CHCH_2OH^* + H^+ + e^- \rightarrow CHCH_2^* + H_2O$). Finally, structural stabilization occurs via C-H bond reorganization and hydrogenation, producing the ethylene precursor $CH_2CH_2^*$ ($CHCH_2^* + H^+ + e^- \rightarrow CH_2CH_2^*$). Subsequently, $CH_2CH_2^*$ continues the hydrogenation reaction to produce $CH_3CH_2^*$ ($CH_2CH_2^* + H^+ + e^- \rightarrow CH_3CH_2^*$). A second H atom then binds to the adjacent carbon, fully saturating the C–C bond to yield ethane ($CH_3CH_3^*$) ($CH_3CH_2^* + H^+ + e^- \rightarrow CH_3CH_3^*$). Throughout this pathway, the synergistic interaction between Pd–Nb bimetallic sites optimizes the electronic environment, accelerating hydrogen migration and bond cleavage. These combined effects drive the highly selective formation of ethane (C_2H_6). The PDS is identified as the transformation of $CH_2CH_2^*$ to $CH_3CH_2^*$ ($U_l = -1.06$ V).

When the polarization direction is switched, the reaction of CORR on Pd–Nb@P↑-In_2Se_3 catalyst [see Fig. 3(b)] is significantly different, with a energetically minimum reaction path of $CO^* \rightarrow CO^*CO^* \rightarrow COCO^* \rightarrow COCOH^* \rightarrow CCO^* \rightarrow CHCO^* \rightarrow CHCHO^* \rightarrow CHCHOH^* \rightarrow CH_2CHOH^* \rightarrow CH_2CH_2OH^* \rightarrow CH_2CH_2^* \rightarrow CH_3CH_2^* \rightarrow CH_3CH_3^*$. Although the final product is also ethane, the PDS is $CH_2CHOH^* \rightarrow CH_2CH_2OH^*$ with the U_l of –1.47 V. The significantly higher overpotential indicates that the reaction efficiency of CORR is polarization tunable via ferroelectric switching. Moreover, the C–C coupling type could also be adjusted by ferroelectric switching. On Pd–Nb@In_2Se_3 catalyst, the C–C coupling type is $CO^*CHO^* \rightarrow COCHO^*$ for the P↓ state, it becomes $CO^*CO^* \rightarrow COCO^*$ for the P↑ state. Notably, the C–C coupling reaction on both P↓ and P↑ states of Pd–Nb@In_2Se_3 catalyst is exothermic reaction. Therefore, in terms of the ability to promote C–C coupling, Pd–Nb@In_2Se_3 catalyst is superior to many catalysts for

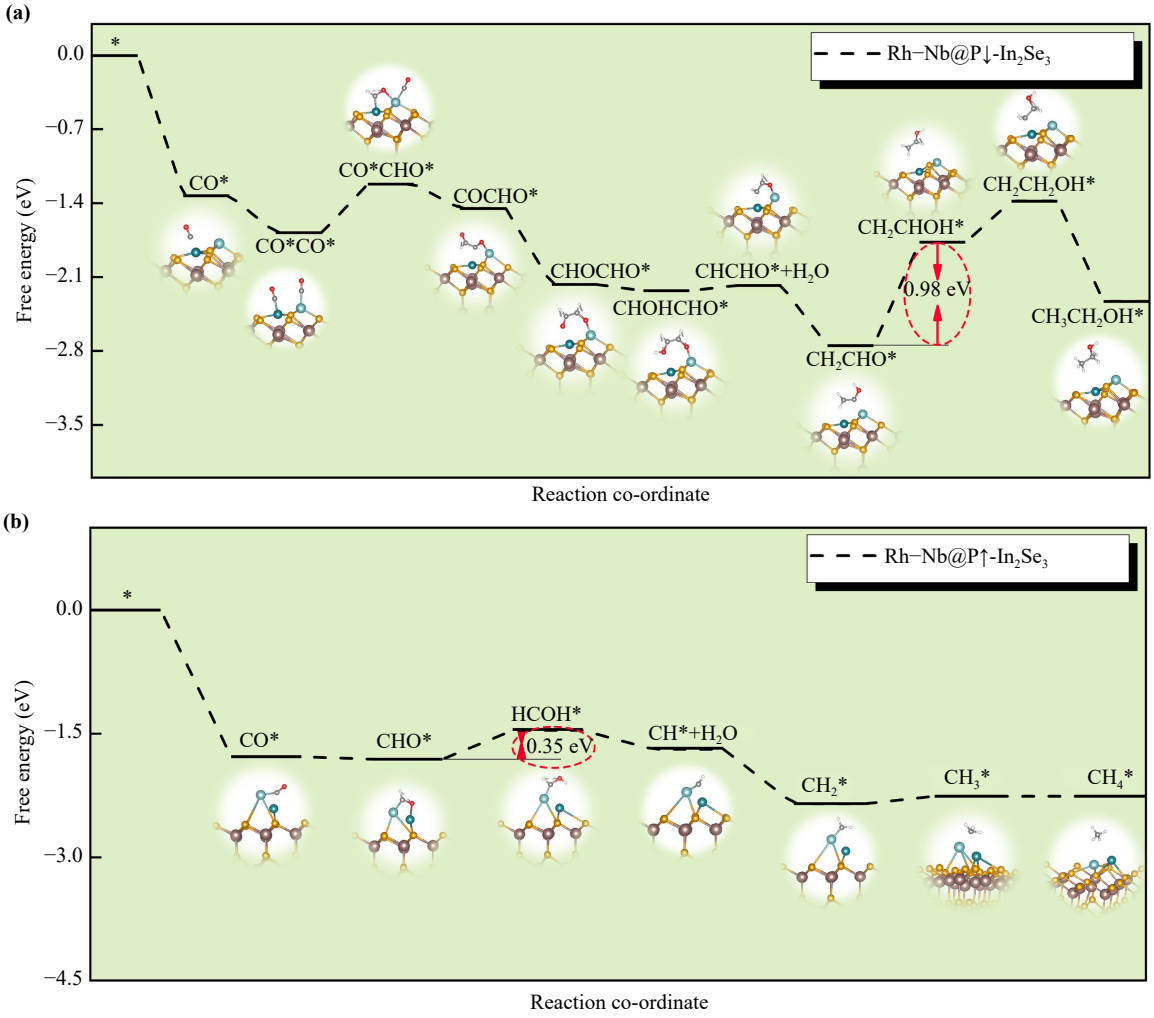

Fig. 4 Free energy distribution of the CORR on **(a)** Rh–Nb@P↓-In_2Se_3 and **(b)** Rh–Nb@P↑-In_2Se_3 along the minimum energy path at 0 V (vs. RHE). The inset shows the optimized configurations of the intermediates.

C_2 products with higher C–C coupling energy barriers, such as θ-Fe_3C(031) (0.99 eV for CH_2+CH_2) [49], Co_2C(001) (0.52 eV for CH_2+CH_2) [50], and χ-Fe_5C_2 (510) (0.96 eV for CH+CH) [51].

To gain deeper insight into the electronic origin of the polarization-dependent C–C coupling behavior, we analyzed the projected density of states and the *d* band centers for the Pd–Nb@In_2Se_3 under both P↓ and P↑ states (see Fig. S5). The results reveal that switching the polarization from P↓ to P↑ induces the *d* band centers of both Pd and Nb shift closer to the Fermi level. This shift signifies an enhanced catalytic activity at both metal sites, which directly rationalizes the facilitated C–C coupling. This point could be verified by the phenomenon that, the released energy of C–C coupling reaction in P↑ state is 0.27 eV more than the one in P↓ state. The *d* band centers shift caused by the polarization switching also change the C–C coupling style, such as CO*CHO*→COCHO* in P↓ state, and CO*CO*→COCO* in P↑ state.

The CORR on Rh–Nb@P↓-In_2Se_3 catalyst follow a minimum reaction path of CO* → CO*CO* → CO*CHO* → COCHO* → CHOCHO* → CHOHCHO* → CHCHO* → CH_2CHO* → CH_2CHOH* → CH_2CH_2OH* → CH_3CH_2OH* [see Fig. 4(a)]. The final product is ethanol, and PDS is CH_2CHO* → CH_2CHOH* with the U_l of –0.98 V. In sharp contrast, CORR over Rh–Nb@P↑-In_2Se_3 catalysts follows a minimum reaction path [see Fig. 4(b)] of CO* → CHO* → HCOH* → CH* → CH_2* → CH_3* → CH_4*. The final product is methane, and the PDS is CHO* → HCOH* with the U_l of –0.35 V. The different limiting potential and final products under different polarization states reveal that, the reaction kinetics and the product selectivity of the CORR can be effectively regulated by adjusting the polarization state of the substrate in ferroelectric DACs.

3.4 Opposite charge center pair promotes C–C coupling

As mentioned before, in Pd–Nb@In_2Se_3 and

Rh–Nb@In_2Se_3, both Pd and Rh single atoms gain electrons from the three Se atoms connected to them, while Nb single atoms lose electrons. In contrast, in the Nb–Nb@In_2Se_3, both Nb atoms lose electrons to surrounding three Se atoms. Therefore, PNCCP can only be formed between the two heteronuclear dual atoms (Pd–Nb, Rh–Nb), but not homonuclear dual atoms (Nb–Nb). In order to investigate whether the PNCCP can lower the C–C coupling energy barrier, CORR on Nb–Nb@P↓-In_2Se_3 is studied for comparison.

As shown in Figs. 3 and 4, the C–C coupling reactions on Pd–Nb@P↓-In_2Se_3, Rh–Nb@P↓-In_2Se_3, and Pd–Nb@P↑-In_2Se_3 are thermodynamically favorable, with the released energies of 0.16, 0.23, and 0.43 eV, respectively. Since the final reaction product on Rh–Nb@P↑-In_2Se_3 tends to be C_1 without C–C coupling process, it is not considered here. As displayed in Fig. S6, the C–C coupling step in Nb–Nb@P↓-In_2Se_3 is CO*CHO*→COCHO* with a energy barrier of 1.28 eV, which is significantly higher than that of Pd–Nb@In_2Se_3 and Rh–Nb@In_2Se_3 with opposite charge center pairs, indicating that the PNCCP favors the occurrence of C–C coupling.

As illustrated in Fig. S7, for the intermediates before C–C coupling reaction, we separately extract the single TM atoms and their attached $C_xH_yO_z$ groups, naming as moiety 1 and moiety 2, respectively. When two moieties possess opposite charges, the Coulomb force between them is attractive with a negative vector value. This attractive force accelerates C–C coupling. A more negative Coulomb force correlates with a lower energy barrier for C–C coupling, thereby facilitating the reaction. Thus, we employ the Coulomb force as a descriptor to quantify the promoting effect of PNCCP on C–C coupling. The Coulomb force (F_{Cou}) could be obtained through the following equation:

$$F_{Cou} = k\frac{q_1 \cdot q_2}{r^2}, \quad (1)$$

where k is electrostatic constant (9×10^9 N·m^2·C^{-2}), r is distance between the gravity centers of moiety 1 and moiety 2, while q_1 and q_2 are the total charge of moiety 1 and moiety 2, respectively. The greater the positive and negative charges on the dual TM single atoms, the more negative the value of the Coulomb force will be. The relationship between Coulomb force and the C–C coupling energy barrier are displayed in Fig. 5. The fitted straight line states that the more negative the value of the Coulomb force is, the smaller the energy barrier for C–C coupling will be, indicating that the C–C coupling reaction will be easier to occur. It is perfectly in line with our expectations, and further substantiates that PNCCP can facilitate the C–C coupling reaction. We note that the linear correlation ($R^2 = 0.82$) has some deviation, primarily arising from the point-charge approximation used in our Coulomb force model, which simplifies the actual diffuse charge distribution.

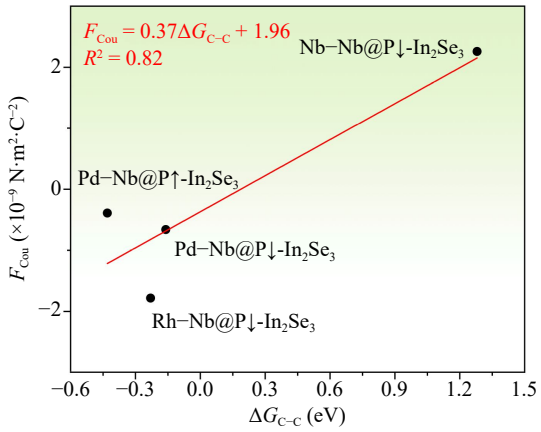

Fig. 5 The Coulomb force (F_{Cou}) between moiety 1 and moiety 2 is proportional to its coupling energy barrier (ΔG_{C-C}). The linear relationship can be described as $F_{Cou} = 0.37 \cdot \Delta G_{C-C} + 1.96$ with a coefficient of determination R^2 of 0.82.

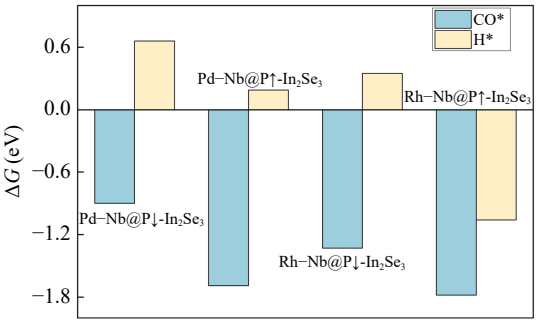

Fig. 6 ΔG_{CO^*} (blue bar) vs. ΔG_{H^*} (yellow bar) on Rh–Nb@In_2Se_3 and Pd–Nb@In_2Se_3 catalysts.

3.5 Selectivity for CORR vs. HER

We also explore the competing relationship between CORR and hydrogen evolution reaction (HER), which as an important side reaction can significantly inhibit the Faraday efficiency of CORR by depleting proton-electron pairs in the electrolyte solution. To check whether CORR is more favorable, the Gibbs free energy changes of the formation of CO* (ΔG_{CO^*}) and H* (ΔG_{H^*}) are firstly calculated. As shown in Fig. 6, the values of ΔG_{CO^*} on both Rh–Nb@In_2Se_3 and Pd–Nb@In_2Se_3 catalysts are smaller than the ones of ΔG_{H^*}. This indicates that the active sites of both Rh–Nb@In_2Se_3 and Pd–Nb@In_2Se_3 catalysts exhibit a higher propensity for adsorbing CO molecules over H atoms, which results in superior CORR selectivity relative to the HER.

4 Conclusion

Our DFT study demonstrates that charge-asymmetric

Pd–Nb and Rh–Nb dual-atom catalysts on ferroelectric In_2Se_3 monolayer provide an efficient and dynamically tunable platform for electrocatalytic CO reduction toward C_2 products. The key to this performance lies in the formation of the PNCCP between the heteronuclear metal sites, which generates a powerful Coulombic attraction, that significantly enables thermodynamically favorable C–C bond formation. The Coulomb force serves as a quantitative descriptor, exhibiting a clear linear relationship, where more negative forces directly correlate with lower C–C coupling energy barriers. Crucially, ferroelectric polarization switching acts as a powerful external knob to reconfigure the electronic structure. By shifting the *d* band centers of the metal sites, polarization reversal not only modulates the reaction energy barriers but also decisively switches the C–C coupling mechanism and the final product selectivity. Furthermore, both Pd–Nb and Rh–Nb dual-atom catalysts exhibit superior affinities for CO adsorption over H adsorption, ensuring high selectivity for CORR against the competing HER. This work predicts ferroelectric DACs as a promising class of electrocatalysts, where the synergistic combination of intrinsic charge asymmetry and external polarization control paves the way for the rational design of highly efficient and electrically tunable systems for on-demand C_2 synthesis.

Declarations The authors declare that they have no competing interests and there are no conflicts.

Electronic supplementary materials The online version contains supplementary material available at https://doi.org/10.15302/frontphys.2026.064202.

Acknowledgements This work was funded by the National Natural Science Foundation of China (Grant Nos. 22573002 and 12504256), the Young Scientist Project of Henan Province (Grant No. 225200810103), the Program for Science & Technology Innovation Talents in Universities of Henan Province (Grant No. 24HASTIT013), the Natural Science Foundation of Henan Province (Grant Nos. 252300420313 and 252300423365), and Henan College Key Research Project (Nos. 24B430005 and 26A430001). Computational resources are provided by the Computational Laboratory for Energy Conversion and Storage.

References

1. X. Zhu, H. Zong, C. J. V. Pérez, H. Miao, W. Sun, Z. Yuan, S. Wang, G. Zeng, H. Xu, Z. Jiang, and G. A. Ozin, Supercharged CO_2 photothermal catalytic methanation: High conversion, rate, and selectivity, *Angew. Chem.* 135(22), e202218694 (2023)
2. X. Zhu, E. Zhou, X. Tai, H. Zong, J. Yi, Z. Yuan, X. Zhao, P. Huang, H. Xu, and Z. Jiang, g-C_3N_4 S-scheme homojunction through van der Waals interface regulation by intrinsic polymerization tailoring for enhanced photocatalytic H_2 evolution and CO_2 reduction, *Angew. Chem. Int. Ed.* 64(13), e202425439 (2025)
3. T. Wang, A. Dong, X. Zhang, R. K. Hocking, and C. Sun, Theoretical study of K_3Sb/graphene heterostructure for electrochemical nitrogen reduction reaction, *Front. Phys. (Beijing)* 17(2), 23501 (2021)
4. L. Ju, Y. Ma, X. Tan, and L. Kou, Controllable electrocatalytic to photocatalytic conversion in ferroelectric heterostructures, *J. Am. Chem. Soc.* 145(48), 26393 (2023)
5. L. Ju, M. Bie, X. Zhang, X. Chen, and L. Kou, Two-dimensional Janus van der Waals heterojunctions: A review of recent research progresses, *Front. Phys. (Beijing)* 16(1), 13201 (2021)
6. Z. Cui, W. Du, C. Xiao, Q. Li, R. Sa, C. Sun, and Z. Ma, Enhancing hydrogen evolution of MoS_2 Basal planes by combining single-boron catalyst and compressive strain, *Front. Phys. (Beijing)* 15(6), 63502 (2020)
7. Q. Kong, X. An, L. Huang, X. Wang, W. Feng, S. Qiu, Q. Wang, and C. Sun, A DFT study of $Ti_3C_2O_2$ MXenes quantum dots supported on single layer graphene: Electronic structure an hydrogen evolution performance, *Front. Phys. (Beijing)* 16(5), 53506 (2021)
8. Q. Li, S. Qiu, and B. Jia, Theoretical investigation of $CoTa_2O_6$/graphene heterojunctions for oxygen evolution reaction, *Front. Phys. (Beijing)* 16(1), 13503 (2020)
9. Q. Kong, X. An, J. Zhang, W. Yao, and C. Sun, Design of heterojunction with components in different dimensions for electrocatalysis applications, *Front. Phys. (Beijing)* 17(4), 43601 (2022)
10. A. Wang, J. Li, and T. Zhang, Heterogeneous single-atom catalysis, *Nat. Rev. Chem.* 2(6), 65 (2018)
11. L. Qi, S. C. Wang, X. Ji, Q. Zhang, X. Xu, B. Liu, L. Li, P. Jing, and J. Zhang, Stabilizing *COOH on Ni single-atom sites by dual-phase $Ni_3ZnC_{0.7}$ and Ni for enhanced electrocatalytic CO_2 reduction, *Inorg. Chem.* 64(20), 10056 (2025)
12. W. Zhu, L. Zhang, S. Liu, A. Li, X. Yuan, C. Hu, G. Zhang, W. Deng, K. Zang, J. Luo, Y. Zhu, M. Gu, Z. J. Zhao, and J. Gong, Enhanced CO_2 electroreduction on neighboring Zn/Co monomers by electronic effect, *Angew. Chem. Int. Ed.* 59(31), 12664 (2020)
13. J. K. Nørskov, J. Rossmeisl, A. Logadottir, L. Lindqvist, J. R. Kitchin, T. Bligaard, and H. Jonsson, Origin of the overpotential for oxygen reduction at a fuel-cell cathode, *J. Phys. Chem. B* 108(46), 17886 (2004)
14. S. Chen, B. Wang, J. Zhu, L. Wang, H. Ou, Z. Zhang, X. Liang, L. Zheng, L. Zhou, Y. Q. Su, D. Wang, and Y. Li, Lewis acid site-promoted single-atomic Cu catalyzes electrochemical CO_2 methanation, *Nano Lett.* 21(17), 7325 (2021)
15. J. M. Heng, H. L. Zhu, Z. H. Zhao, D. S. Huang, J. Y. Li, P. Q. Liao, and X. M. Chen, A conductive dinuclear cuprous complex mimicking the active edge site of the Copper(100)/(111) plane for selective electroreduction of CO_2 to C_2H_4 at industrial current density, *Research* 2022, 0008 (2022)
16. H. Wang, X. Bi, Y. Yan, Y. Zhao, Z. Yang, H. Ning, and M. Wu, Efficient electrocatalytic reduction of CO_2 to ethanol enhanced by spacing effect of Cu–Cu in $Cu_{2-x}Se$ nanosheets, *Adv. Funct. Mater.* 33(25), 2214946

(2023)
17. Y. Ren, W. Cen, L. Yang, L. Ye, J. Liu, and D. Sun, Synergistic cooperation of active sites in Cu-incorporated nitrogen-doped porous carbon for CO_2 electroreduction to ethanol, *Inorg. Chem.* 64(23), 11658 (2025)
18. A. Vasileff, Y. Zhu, X. Zhi, Y. Zhao, L. Ge, H. M. Chen, Y. Zheng, and S. Z. Qiao, Electrochemical reduction of CO_2 to ethane through stabilization of an ethoxy intermediate, *Angew. Chem. Int. Ed.* 59(44), 19649 (2020)
19. H. Wang, Y. K. Tzeng, Y. Ji, Y. Li, J. Li, X. Zheng, A. Yang, Y. Liu, Y. Gong, L. Cai, Y. Li, X. Zhang, W. Chen, B. Liu, H. Lu, N. A. Melosh, Z. X. Shen, K. Chan, T. Tan, S. Chu, and Y. Cui, Synergistic enhancement of electrocatalytic CO_2 reduction to C_2 oxygenates at nitrogen-doped nanodiamonds/Cu interface, *Nat. Nanotechnol.* 15(2), 131 (2020)
20. M. Wang, Y. Xiang, Y. Lin, Y. Sun, Z. Zhu, S. Wu, and X. Cao, p–d Orbital coupling in silicon-based dual-atom catalysts for enhanced CO_2 reduction: insight into electron regulation of active center and coordination atoms, *J. Mater. Chem. A* 12(46), 31902 (2024)
21. X. D. Zhang, K. Liu, J. W. Fu, H. M. Li, H. Pan, J. H. Hu, and M. Liu, Pseudo-copper Ni–Zn alloy catalysts for carbon dioxide reduction to C_2 products, *Front. Phys. (Beijing)* 16(6), 63500 (2021)
22. Y. Jia, F. Li, K. Fan, and L. Sun, Cu-based bimetallic electrocatalysts for CO_2 reduction, *Advanced Powder Materials* 1(1), 100012 (2022)
23. Y. Ma, S. Liu, J. Mao, M. Sun, K. Shi, W. Li, W. Zhao, J. Shan, Y. Zhao, Z. Jiang, R. Zhang, R. Gao, W. Liu, B. Huang, G. Q. M. Lu, J. Liu, and L. Wu, Ligand-restricted synthesis of highly paired dual-atom catalysts, *Nat. Mater.*, doi: 10.1038/s41563-025-02385-6 (2025)
24. J. M. Heng, H. L. Zhu, Z. H. Zhao, P. Q. Liao, and X. M. Chen, Fabrication of ultrahigh-loading dual copper sites in nitrogen-doped porous carbons boosting electroreduction of CO_2 to C_2H_4 under neutral conditions, *Adv. Mater.* 37(4), 2415101 (2025)
25. H. Shi, H. Wang, Y. Zhou, J. Li, P. Zhai, X. Li, G. G. Gurzadyan, J. Hou, H. Yang, and X. Guo, Atomically dispersed indium-copper dual-metal active sites promoting C–C coupling for CO_2 photoreduction to ethanol, *Angew. Chem.* 134(40), e202208904 (2022)
26. G. Jia, M. Sun, Y. Wang, Y. Shi, L. Zhang, X. Cui, B. Huang, and J. C. Yu, Asymmetric coupled dual-atom sites for selective photoreduction of carbon dioxide to acetic acid, *Adv. Funct. Mater.* 32(41), 2206817 (2022)
27. X. Bai, Q. Li, L. Shi, X. Niu, C. Ling, and J. Wang, Hybrid Cu^0 and Cu^{x+} as atomic interfaces promote high-selectivity conversion of CO_2 to C_2H_5OH at low potential, *Small* 16(12), 1901981 (2020)
28. S. Zhu, X. Li, X. Jiao, W. Shao, L. Li, X. Zu, J. Hu, J. Zhu, W. Yan, C. Wang, Y. Sun, and Y. Xie, Selective CO_2 photoreduction into C_2 product enabled by charge-polarized metal pair sites, *Nano Lett.* 21(5), 2324 (2021)
29. Y. Zhou, F. Che, M. Liu, C. Zou, Z. Liang, P. De Luna, H. Yuan, J. Li, Z. Wang, H. Xie, H. Li, P. Chen, E. Bladt, R. Quintero-Bermudez, T. K. Sham, S. Bals, J. Hofkens, D. Sinton, G. Chen, and E. H. Sargent, Dopant-induced electron localization drives CO_2 reduction to C_2 hydrocarbons, *Nat. Chem.* 10(9), 974 (2018)
30. J. Wang, Z. Huang, W. Liu, C. Chang, H. Tang, Z. Li, W. Chen, C. Jia, T. Yao, S. Wei, Y. Wu, and Y. Li, Design of N-coordinated dual-metal sites: A stable and active Pt-free catalyst for acidic oxygen reduction reaction, *J. Am. Chem. Soc.* 139(48), 17281 (2017)
31. W. Ren, X. Tan, W. Yang, C. Jia, S. Xu, K. Wang, S. C. Smith, and C. Zhao, Isolated diatomic Ni–Fe metal-nitrogen sites for synergistic electroreduction of CO_2, *Angew. Chem. Int. Ed.* 58(21), 6972 (2019)
32. L. Zhang, J. M. T. A. Fischer, Y. Jia, X. Yan, W. Xu, X. Wang, J. Chen, D. Yang, H. Liu, L. Zhuang, M. Hankel, D. J. Searles, K. Huang, S. Feng, C. L. Brown, and X. Yao, Coordination of atomic Co–Pt coupling species at carbon defects as active sites for oxygen reduction reaction, *J. Am. Chem. Soc.* 140(34), 10757 (2018)
33. D. Li, M. H. Zhao, J. Garra, A. M. Kolpak, A. M. Rappe, D. A. Bonnell, and J. M. Vohs, Direct in situ determination of the polarization dependence of physisorption on ferroelectric surfaces, *Nat. Mater.* 7(6), 473 (2008)
34. L. Ju, J. Shang, X. Tang, and L. Kou, Tunable photocatalytic water splitting by the ferroelectric switch in a 2D $AgBiP_2Se_6$ monolayer, *J. Am. Chem. Soc.* 142(3), 1492 (2020)
35. L. Ju, X. Tan, X. Mao, Y. Gu, S. Smith, A. Du, Z. Chen, C. Chen, and L. Kou, Controllable CO_2 electrocatalytic reduction via ferroelectric switching on single atom anchored In_2Se_3 monolayer, *Nat. Commun.* 12(1), 5128 (2021)
36. G. Kresse and J. Furthmüller, Efficient iterative schemes for ab initio total-energy calculations using a plane-wave basis set, *Phys. Rev. B* 54(16), 11169 (1996)
37. G. Kresse and J. Furthmüller, Efficiency of ab-initio total energy calculations for metals and semiconductors using a plane-wave basis set, *Comput. Mater. Sci.* 6(1), 15 (1996)
38. P. E. Blöchl, Projector augmented-wave method, *Phys. Rev. B* 50(24), 17953 (1994)
39. G. Kresse and D. Joubert, From ultrasoft pseudopotentials to the projector augmented-wave method, *Phys. Rev. B* 59(3), 1758 (1999)
40. J. P. Perdew, K. Burke, and M. Ernzerhof, Generalized gradient approximation made simple, *Phys. Rev. Lett.* 77(18), 3865 (1996)
41. S. Grimme, Semiempirical GGA-type density functional constructed with a long-range dispersion correction, *J. Comput. Chem.* 27(15), 1787 (2006)
42. J. Zhang, X. Tang, M. Chen, D. Ma, and L. Ju, Tunable photocatalytic water splitting performance of armchair MoSSe nanotubes realized by polarization engineering, *Inorg. Chem.* 61(43), 17353 (2022)
43. X. Mao, G. Kour, L. Zhang, T. He, S. Wang, C. Yan, Z. Zhu, and A. Du, Silicon-doped graphene edges: an efficient metal-free catalyst for the reduction of CO_2 into methanol and ethanol, *Catal. Sci. Technol.* 9(23), 6800 (2019)
44. Y. Zhou, D. Wu, Y. Zhu, Y. Cho, Q. He, X. Yang, K. Herrera, Z. Chu, Y. Han, M. C. Downer, H. Peng, and K. Lai, Out-of-plane piezoelectricity and ferroelectricity

in layered alpha-In_2Se_3 nanoflakes, *Nano Lett.* 17(9), 5508 (2017)

45. W. Ding, J. Zhu, Z. Wang, Y. Gao, D. Xiao, Y. Gu, Z. Zhang, and W. Zhu, Prediction of intrinsic two-dimensional ferroelectrics in In_2Se_3 and other III_2-VI_3 van der Waals materials, *Nat. Commun.* 8(1), 14956 (2017)
46. L. Zhang, R. Si, H. Liu, N. Chen, Q. Wang, K. Adair, Z. Wang, J. Chen, Z. Song, J. Li, M. N. Banis, R. Li, T. K. Sham, M. Gu, L. M. Liu, G. A. Botton, and X. Sun, Atomic layer deposited Pt–Ru dual-metal dimers and identifying their active sites for hydrogen evolution reaction, *Nat. Commun.* 10(1), 4936 (2019)
47. T. Tang, Y. Wang, J. Han, Q. Zhang, X. Bai, X. Niu, Z. Wang, and J. Guan, Dual-atom Co–Fe catalysts for oxygen reduction reaction, *Chin. J. Catal.* 46, 48 (2023)
48. C. Chen, M. Sun, K. Wang, and Y. Li, Dual-metal single-atomic catalyst: The challenge in synthesis, characterization, and mechanistic investigation for electrocatalysis, *SmartMat* 3(4), 533 (2022)
49. Y. Wang, Y. Li, S. Huang, J. Wang, H. Wang, J. Lv, and X. Ma, Insight into CH_4 formation and chain growth mechanism of Fischer–Tropsch synthesis on θ-Fe_3C(031), *Chem. Phys. Lett.* 682, 115 (2017)
50. J. Cheng, P. Hu, P. Ellis, S. French, G. Kelly, and C. M. Lok, Density functional theory study of iron and cobalt carbides for Fischer–Tropsch synthesis, *J. Phys. Chem. C* 114(2), 1085 (2010)
51. T. H. Pham, Y. Qi, J. Yang, X. Duan, G. Qian, X. Zhou, D. Chen, and W. Yuan, Insights into Hägg iron-carbide-catalyzed Fischer–Tropsch synthesis: Suppression of CH_4 formation and enhancement of C–C coupling on χ-Fe_5C_2 (510), *ACS Catal.* 5(4), 2203 (2015)